



Visual Orbits of Spectroscopic Binaries with the CHARA Array. III. HD 8374 and HD 24546

Kathryn V. Lester¹ , Francis C. Fekel² , Matthew Mutterspaugh³, Douglas R. Gies¹ , Gail H. Schaefer⁴ , Christopher D. Farrington⁴ , Zhao Guo⁵ , Rachel A. Matson^{6,7} , John D. Monnier⁸ , Theo ten Brummelaar⁴ , Judit Sturmann⁴ , and Samuel A. Weiss⁹

¹ Center for High Angular Resolution Astronomy and Department of Physics & Astronomy, Georgia State University, Atlanta, GA 30302, USA; lester@astro.gsu.edu

² Center of Excellence in Information Systems, Tennessee State University, Nashville, TN 37209, USA

³ Division of Science, Technology, & Mathematics, Columbia State Community College, Columbia, TN 38401, USA

⁴ The CHARA Array of Georgia State University, Mount Wilson Observatory, Mount Wilson, CA 91023, USA

⁵ Department of Astronomy & Astrophysics, Pennsylvania State University, University Park, PA 16802, USA

⁶ NASA Ames Research Center, Moffett Field, CA 94035, USA

⁷ U.S. Naval Observatory, Washington, DC 20392, USA

⁸ Department of Astronomy, University of Michigan, Ann Arbor, MI 48109, USA

⁹ Department of Physics, Southern Connecticut State University, New Haven, CT 06515, USA

Received 2020 April 4; revised 2020 April 29; accepted 2020 April 30; published 2020 July 9

Abstract

We present the visual orbits of two long-period spectroscopic binary stars, HD 8374 and HD 24546, using interferometric observations acquired with the CHARA Array and the Palomar Testbed Interferometer. We also obtained new radial velocities from echelle spectra using the APO 3.5 m and Fairborn 2.0 m telescopes. By combining the visual and spectroscopic observations, we solve for the full, three-dimensional orbits and determine the stellar masses and distances to within 3% uncertainty. We then estimate the effective temperature and radius of each component star through Doppler tomography and spectral energy distribution analyses, in order to compare the observed stellar parameters to the predictions of stellar evolution models. For HD 8374, we find masses of $M_1 = 1.636 \pm 0.050 M_{\odot}$ and $M_2 = 1.587 \pm 0.049 M_{\odot}$, radii of $R_1 = 1.84 \pm 0.05 R_{\odot}$ and $R_2 = 1.66 \pm 0.12 R_{\odot}$, temperatures of $T_{\text{eff}\,1} = 7280 \pm 110$ K and $T_{\text{eff}\,2} = 7280 \pm 120$ K, and an estimated age of 1.0 Gyr. For HD 24546, we find masses of $M_1 = 1.434 \pm 0.014 M_{\odot}$ and $M_2 = 1.409 \pm 0.014 M_{\odot}$, radii of $R_1 = 1.67 \pm 0.06 R_{\odot}$ and $R_2 = 1.60 \pm 0.10 R_{\odot}$, temperatures of $T_{\text{eff}\,1} = 6790 \pm 120$ K and $T_{\text{eff}\,2} = 6770 \pm 90$ K, and an estimated age of 1.4 Gyr. HD 24546 is therefore too old to be a member of the Hyades cluster, despite its physical proximity to the group.

Unified Astronomy Thesaurus concepts: Spectroscopic binary stars (1557); Visual binary stars (1777); Fundamental parameters of stars (555)

Supporting material: figure sets

1. Introduction

We are continuing our series of papers measuring the visual orbits of spectroscopic binary stars with interferometry (Lester et al. 2019a, 2019b), in order to determine the fundamental stellar parameters of the components and test the predictions of stellar evolution models. In this paper, we present the results for two long-period binaries, HD 8374 and HD 24546. HD 8374¹⁰ contains a pair of late A-type stars with an orbital period of 35 days. The first spectroscopic orbit was completed by Fletcher (1967), then recently updated using high-resolution data by Fekel et al. (2011). HD 8374 is also classified as a metallic line (Am) star due to its weak Ca II H & K lines (Abt & Morrell 1995).

HD 24546¹¹ contains a pair of F5 stars with an orbital period of 30 days. Spectroscopic orbits were determined by Wallerstein (1973) and Abt & Levy (1976). HD 24546 also has a possible third companion (43 Per B¹²) at a separation of 75'' (Abt & Levy 1976; Tokovinin 1997) with a proper motion

and parallax similar to HD 24546 (Lépine & Bongiorno 2007; Montes et al. 2018). Even if 43 Per B is physically associated with HD 24546, it is outside the field of view of our telescopes and would not cause perturbations in the orbit of HD 24546 due to the estimated orbital period of 95,000 yr (Tokovinin 1997). Some investigators have reported that HD 24546 is a member of the Hyades cluster (Eggen 1971; Montes et al. 2018), while others found that it is not (Perryman et al. 1998), so measuring accurate masses and age for this system will verify or refute cluster membership.

In Section 2, we describe our spectroscopic observations and radial velocities. In Section 3, we describe our interferometric observations, binary positions, and combined orbital solution. In Section 4, we determine the fundamental stellar parameters of each component and compare the results to stellar evolution models. We further discuss our results in Section 5.

2. Spectroscopy

2.1. APO Observations

We observed HD 8374 and HD 24546 with the ARC echelle spectrograph (ARCES; Wang et al. 2003) on the APO 3.5 m telescope from 2015 to 2020. Our observations are listed in Table 1 for HD 8374 and Table 2 for HD 24546. ARCES

¹⁰ 47 And, HR 395; $V = 5.6$ mag; $\alpha = 01^{\circ}23'40.6'', \delta = +37^{\circ}42'53.8''$ (J2000).

¹¹ 43 Per A, BD +50 860, HR 1210; $V = 5.3$ mag; $\alpha = 03^{\circ}56'36.6'', \delta = +50^{\circ}41'43.4''$ (J2000).

¹² 43 Per B, BD +50 861; $V = 10.5$ mag; $\alpha = 03^{\circ}56'40.7'', \delta = +50^{\circ}42'47.5''$ (J2000).

Table 1
Radial Velocity Measurements for HD 8374

UT Date	HJD-2,400,000	Orbital Phase	V_{r1} (km s $^{-1}$)	σ_1 (km s $^{-1}$)	$O - C$ (km s $^{-1}$)	V_{r2} (km s $^{-1}$)	σ_2 (km s $^{-1}$)	$O - C$ (km s $^{-1}$)	Source
2011 Mar 3	55623.6328	0.61	-1.60	0.32	-0.41	29.80	0.29	-0.15	Fairborn
2011 May 20	55701.9727	0.83	-3.70	0.32	0.03	32.80	0.29	0.24	Fairborn
2011 Oct 11	55845.6211	0.89	0.10	0.32	-0.22	28.30	0.29	-0.08	Fairborn
2011 Dec 27	55922.5820	0.06	53.50	0.32	0.16	-26.50	0.29	-0.24	Fairborn
2012 Jun 21	56099.9141	0.08	48.10	0.32	0.15	-20.60	0.29	0.11	Fairborn
2012 Sep 1	56171.9648	0.12	37.20	0.32	0.20	-9.70	0.29	-0.28	Fairborn
2012 Oct 2	56202.6953	0.98	55.10	0.32	0.11	-27.90	0.29	0.06	Fairborn
2012 Oct 30	56230.8945	0.78	-4.80	0.32	-0.55	33.00	0.29	-0.10	Fairborn
2013 Feb 10	56333.6953	0.69	-3.40	0.32	-0.29	32.10	0.29	0.18	Fairborn
2013 May 22	56434.9688	0.55	0.20	0.32	-0.52	27.90	0.29	-0.07	Fairborn
2013 Sep 6	56541.7578	0.57	0.30	0.32	0.22	28.90	0.29	0.26	Fairborn
2013 Nov 26	56622.8203	0.86	-2.10	0.32	0.03	31.00	0.29	0.09	Fairborn
2013 Dec 26	56652.5859	0.70	-3.60	0.32	-0.17	32.30	0.29	0.05	Fairborn
2014 May 28	56805.9492	0.04	64.20	0.32	-0.17	-37.80	0.29	-0.17	Fairborn
2014 Jun 26	56834.9609	0.86	-2.30	0.32	-0.04	30.80	0.29	-0.25	Fairborn
2014 Oct 1	56931.7422	0.60	-0.80	0.32	-0.05	29.50	0.29	0.00	Fairborn
2014 Nov 16	56977.6133	0.89	1.20	0.32	0.07	27.70	0.29	0.15	Fairborn
2015 Jun 7	57180.9258	0.64	-2.00	0.32	0.04	31.00	0.29	0.18	Fairborn
2015 Nov 10	57336.6836	0.05	61.70	0.23	0.23	-34.10	0.27	0.54	Fairborn
2015 Dec 1	57357.6445	0.64	-1.81	1.10	0.13	30.03	1.18	-0.69	APO
2016 Feb 18	57436.6680	0.87	-1.20	0.23	0.09	30.20	0.27	0.15	Fairborn
2016 Aug 7	57607.9570	0.72	-3.30	0.23	0.34	32.50	0.27	0.03	Fairborn
2016 Sep 14	57645.7852	0.79	-3.85	1.08	0.39	32.33	1.19	-0.76	APO
2016 Oct 14	57675.8672	0.64	-2.00	0.23	-0.12	30.90	0.27	0.25	Fairborn
2016 Oct 15	57676.6016	0.66	-2.89	1.12	-0.49	29.09	1.25	-2.11	APO
2016 Oct 21	57682.7852	0.83	-3.24	1.09	0.34	31.26	1.20	-1.15	APO
2016 Nov 18	57710.8008	0.62	-1.40	0.23	0.14	30.20	0.27	-0.11	Fairborn
2016 Nov 19	57711.6445	0.65	-2.23	1.08	-0.06	29.20	1.22	-1.76	APO
2017 Jan 6	57759.7773	0.01	74.10	0.23	0.05	-47.80	0.27	-0.19	Fairborn
2017 May 17	57890.9727	0.72	-3.90	0.23	-0.23	32.70	0.27	0.20	Fairborn
2017 Jun 30	57934.9219	0.96	28.80	0.23	-0.09	-1.10	0.27	-0.04	Fairborn
2017 Aug 30	57995.9961	0.69	-2.80	0.23	0.30	31.80	0.27	-0.12	Fairborn
2017 Sep 2	57998.7617	0.77	-4.04	1.09	0.17	32.09	1.20	-0.96	APO
2017 Oct 4	58030.7109	0.67	-2.60	0.23	0.09	31.80	0.27	0.30	Fairborn
2017 Nov 9	58066.6758	0.69	-3.00	0.23	0.07	32.20	0.27	0.32	Fairborn
2017 Dec 27	58114.6133	0.04	64.93	0.53	1.05	-35.67	0.58	1.46	APO
2018 Sep 27	58388.7539	0.79	-2.34	1.16	1.88	33.75	1.30	0.68	APO
2019 Jan 14	58497.5898	0.87	-0.59	1.05	1.02	30.19	1.19	-0.18	APO
2019 Jan 21	58504.7109	0.07	50.80	0.23	0.19	-23.20	0.27	0.25	Fairborn
2019 Jan 22	58505.5664	0.10	42.12	0.52	-0.25	-15.14	0.58	-0.19	APO
2019 Aug 18	58713.9609	0.99	58.81	0.54	0.04	-31.52	0.60	0.34	APO
2019 Sep 13	58739.9023	0.72	-2.79	1.14	0.93	32.03	1.27	-0.51	APO
2019 Oct 21	58777.8125	0.79	-3.21	1.06	1.01	32.85	1.18	-0.22	APO

covers 3500–10500 Å over 107 orders at an average resolving power of $R = 30,000$. We reduced our data using standard echelle procedures in IRAF, then removed the blaze function using the procedure in Appendix A of Kolbas et al. (2015). Radial velocities (V_r) for the APO data were measured with the multi-order TODCOR method (Zucker & Mazeh 1994; Zucker et al. 2003) as described in Lester et al. (2019a). Briefly, TODCOR calculates the cross correlation function (CCF) for a grid of primary and secondary radial velocities. BLUERED model spectra (Bertone et al. 2008) were created as template spectra based on atmospheric parameters from Fekel et al. (2011) for HD 8374 and from Wallerstein (1973) for HD 24546. The CCFs for each echelle order were then added together to find the maximum CCF and corresponding best-fit radial velocities. TODCOR also estimates the monochromatic flux ratio near H α to be $f_2 / f_1 = 0.91 \pm 0.12$ for HD 8374 and $f_2 / f_1 = 0.98 \pm 0.10$ for HD 24546.

2.2. Fairborn Observations

We also acquired spectroscopic observations of HD 8374 and HD 24546 at Fairborn Observatory in southeast Arizona with the Tennessee State University 2.0 m Automatic Spectroscopic Telescope (AST) and a fiber-fed echelle spectrograph (Eaton & Williamson 2004). The new AST observations of HD 8374 from 2011 to 2019 are listed in Table 1 and are a continuation of those published by Fekel et al. (2011). The observations of HD 24546 acquired between 2003 and 2019 are listed in Table 2. All observations through the spring of 2011 were acquired with a 2048×4096 SITe ST-002A CCD. Those spectra have 21 orders, cover a wavelength region of 4920–7100 Å, and have a resolving power of 35,000 at 6000 Å. During the summer of 2011 we replaced the SITe CCD with a Fairchild 486 CCD that has a 4096×4096 pixel array enabling coverage of a wavelength range of 3800–8600 Å over 48 orders (Fekel et al. 2013). We used a 200 μm fiber that produced a resolving power of 25,000 at

Table 2
Radial Velocity Measurements for HD 24546

UT Date	HJD-2,400,000	Orbital Phase	V_{r1} (km s $^{-1}$)	σ_1 (km s $^{-1}$)	$O - C$ (km s $^{-1}$)	V_{r2} (km s $^{-1}$)	σ_2 (km s $^{-1}$)	$O - C$ (km s $^{-1}$)	Source
2003 Nov 26	52970.0430	0.41	45.70	0.26	0.59	5.49	0.25	0.08	Fairborn
2004 Oct 12	53291.0273	0.96	-44.73	0.26	-0.21	96.74	0.25	0.15	Fairborn
2004 Nov 13	53322.9648	0.01	-36.89	0.26	-0.02	88.71	0.25	-0.11	Fairborn
2004 Dec 13	53352.9688	0.99	-52.89	0.26	0.10	105.29	0.25	0.08	Fairborn
2004 Dec 14	53353.9219	0.02	-11.73	0.26	0.16	63.33	0.25	-0.07	Fairborn
2004 Dec 20	53359.9219	0.22	48.01	0.26	0.29	2.88	0.25	0.12	Fairborn
2005 Apr 14	53474.6875	0.99	-53.63	0.26	0.16	106.05	0.25	0.03	Fairborn
2005 Nov 11	53686.0156	0.93	-28.00	0.26	0.01	79.33	0.25	-0.47	Fairborn
2006 Feb 13	53779.8125	0.02	-23.95	0.26	-0.04	75.90	0.25	0.27	Fairborn
2006 Mar 26	53820.6992	0.36	47.00	0.26	0.40	4.29	0.25	0.39	Fairborn
2006 Apr 21	53846.6680	0.21	48.44	0.26	0.88	3.22	0.25	0.30	Fairborn
2016 Jan 26	57413.6328	0.40	45.66	0.98	0.07	5.28	0.86	0.36	APO
2016 Oct 21	57682.7812	0.24	47.43	1.00	-0.49	2.35	0.86	-0.21	APO
2016 Nov 19	57711.6602	0.19	46.26	0.96	-0.59	3.35	0.83	-0.29	APO
2016 Dec 15	57737.6445	0.04	8.36	1.01	0.18	43.09	0.93	0.11	APO
2017 Jan 11	57764.8633	0.94	-29.54	0.36	-0.65	79.67	0.31	-1.03	APO
2017 Dec 27	58114.6445	0.43	45.12	0.97	0.48	6.54	0.87	0.65	APO
2018 Jan 28	58146.8242	0.48	41.78	0.96	-0.70	7.49	0.86	-0.60	APO
2018 Sep 27	58388.7695	0.43	44.47	1.09	0.02	6.29	0.98	0.19	APO
2018 Dec 24	58476.6680	0.32	47.95	0.99	0.55	3.99	0.84	0.90	APO
2019 Jan 14	58497.5977	0.01	-34.84	0.36	0.69	87.64	0.31	0.19	APO
2019 Jan 15	58498.6328	0.04	9.18	1.12	0.47	42.24	1.02	-0.21	APO
2019 Jan 19	58502.8281	0.18	46.81	0.97	0.30	4.62	0.83	0.64	APO
2019 Jan 22	58505.5391	0.27	47.19	1.07	-0.76	1.82	0.94	-0.70	APO
2019 Mar 24	58566.5859	0.27	47.41	1.00	-0.51	2.23	0.86	-0.32	APO
2019 Sep 13	58739.9375	0.97	-51.78	0.37	0.51	105.06	0.32	0.56	APO
2019 Sep 19	58745.7422	0.16	45.26	0.26	-0.15	4.95	0.25	-0.16	Fairborn
2019 Oct 9	58765.6914	0.82	13.70	0.26	-0.06	36.93	0.25	-0.37	Fairborn
2019 Oct 14	58770.8164	0.98	-56.40	0.37	0.04	108.78	0.32	0.05	APO
2019 Oct 20	58776.7461	0.18	46.36	0.26	-0.11	3.81	0.25	-0.22	Fairborn
2019 Oct 21	58777.6445	0.21	47.30	0.26	-0.17	2.72	0.25	-0.29	Fairborn
2019 Oct 21	58777.8789	0.22	48.35	0.96	0.72	3.92	0.81	1.07	APO
2019 Oct 25	58781.6289	0.34	47.08	0.26	0.04	3.11	0.25	-0.34	Fairborn
2019 Oct 29	58785.6875	0.47	43.08	0.26	0.12	7.40	0.25	-0.20	Fairborn
2019 Oct 30	58786.6250	0.50	41.42	0.26	-0.24	8.50	0.25	-0.43	Fairborn
2019 Oct 31	58787.6250	0.54	40.16	0.26	0.05	10.57	0.25	0.07	Fairborn
2019 Nov 1	58788.6250	0.57	38.44	0.26	0.06	12.12	0.25	-0.14	Fairborn
2019 Nov 9	58796.8359	0.84	8.89	0.26	-0.10	41.97	0.25	-0.19	Fairborn
2019 Nov 13	58800.8359	0.97	-52.84	0.26	-0.17	104.75	0.25	-0.14	Fairborn
2019 Nov 14	58801.8359	0.00	-42.44	0.26	-0.05	94.60	0.25	0.17	Fairborn
2019 Nov 14	58801.8906	0.00	-39.35	0.34	0.63	92.01	0.30	0.03	APO
2019 Nov 15	58802.8359	0.04	2.28	0.26	-0.32	48.49	0.25	-0.17	Fairborn
2019 Nov 17	58804.8359	0.10	37.63	0.26	-0.11	12.91	0.25	-0.00	Fairborn
2019 Nov 18	58805.8359	0.13	43.19	0.26	0.10	7.34	0.25	-0.13	Fairborn
2019 Nov 23	58810.8086	0.30	47.79	0.26	0.07	2.73	0.25	-0.03	Fairborn
2020 Jan 12	58860.6758	0.94	-28.98	0.34	0.20	80.93	0.30	-0.07	APO

6000 Å. Eaton & Williamson (2007) explained the reduction and wavelength calibration of the raw AST spectra.

Fekel et al. (2009) provided a general description of the typical velocity reduction. For the two stars in this work, we used a solar-type star line list consisting of 168 lines in the wavelength region 4920–7100 Å. Each line was fitted with a rotational broadening function (Sandberg Lacy & Fekel 2011), and when the lines of the two components were blended we obtained a simultaneous fit. The stellar velocity was determined as the average of the line fits. A value of 0.3 km s $^{-1}$ was added to the SITe CCD velocities and 0.6 km s $^{-1}$ to the Fairchild CCD velocities to make the resulting velocities from the two CCDs consistent with the velocity zero-point of Scarfe (2010).

2.3. Preliminary Spectroscopic Orbit

To account for differences in the zero-point offsets of the APO and Fairborn spectrographs, we first fit separate orbital solutions to each data set using the RVFIT program¹³ (Iglesias-Marzoa et al. 2015) to solve for the spectroscopic orbital parameters: the orbital period (P), epoch of periastron (T), eccentricity (e), longitude of periastron of the primary star (ω_1), systemic velocity (γ), and the velocity semi-amplitudes (K_1 , K_2). We found offsets of -0.14 km s $^{-1}$ and -0.20 km s $^{-1}$ for the ARCES data of HD 8374 and HD 24546, respectively, in order to match the systemic velocities to those of the Fairborn data.

¹³ <http://www.cefca.es/people/~rigleas/rvfit.html>

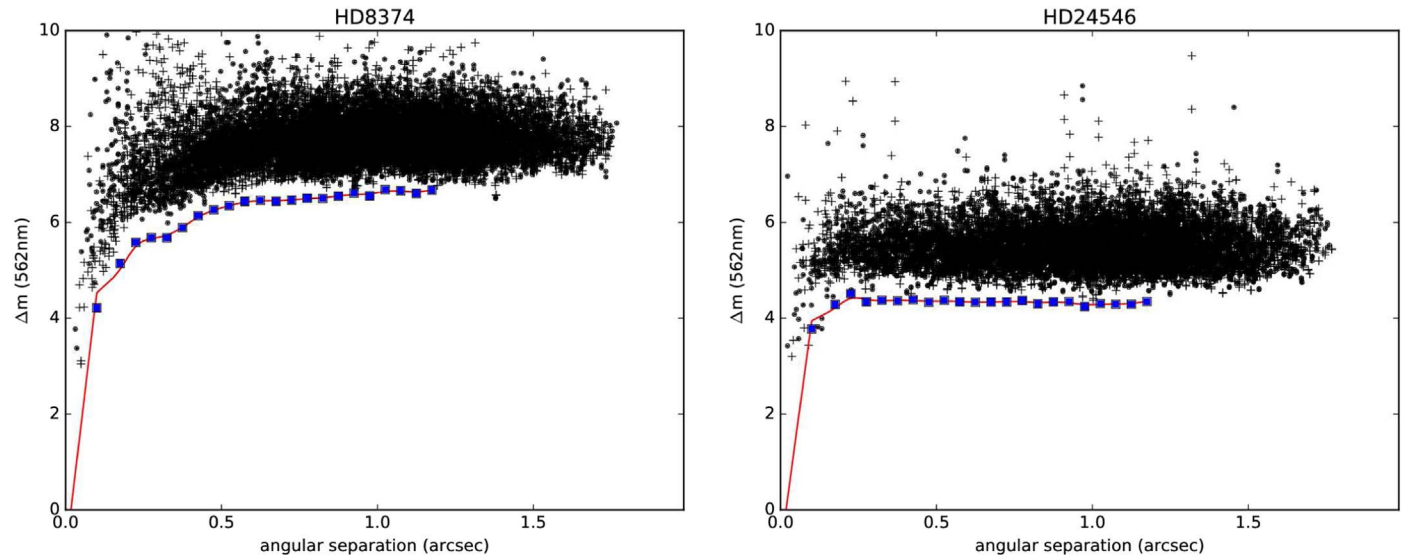


Figure 1. Background sensitivity curves as a function of radius from the center for the reconstructed speckle images. The black points represent the local maxima (crosses) and minima (dots). The blue squares mark the 5σ background sensitivity limit within $0.^{\circ}05$ bins, and the red line corresponds to a spline fit (Horch et al. 2017). No points fall below the contrast limits, therefore no tertiary companions were detected for HD 8374 or HD 24546.

We also fit an orbit to the previously published velocities of HD 8374 from Fekel et al. (2011) using preliminary uncertainties equal to $1/\sqrt{\text{weight}}$. We then used the χ^2 values from the individual APO, Fairborn, and Fekel et al. (2011) solutions to rescale the uncertainties such that the reduced χ^2 of each data set equals one. The adjusted APO velocities and the rescaled uncertainties for the APO and new Fairborn data are listed in Tables 1 and 2, along with the residuals from the combined (VB+SB2) orbital solutions found in Section 3.5.

3. Interferometry

3.1. ‘Alopeke Observations

We observed these stars on 2018 October 23 with the ‘Alopeke speckle camera (Scott et al. 2018) on the 8.0 m Gemini-North telescope¹⁴ in order to search for any unresolved companions outside of CHARA’s limits that would bias our results. ‘Alopeke takes a series of 1000 60 ms exposures simultaneously in the 562 and 716 nm bands, and the data were reduced with the speckle team’s pipeline (Howell et al. 2011). We searched for companions within $1.^{\circ}5$ using the method given by Horch et al. (2017), but found no hidden companions down to the detection limits of $\Delta m < 6$ mag for HD 8374 and $\Delta m < 4$ mag for HD 24546. Plots of the detection limits for the 562 nm filter are shown in Figure 1.

3.2. CHARA Array Observations

We observed HD 8374 and HD 24546 with the CHARA Array from 2017 to 2019. CHARA has six 1.0 m telescopes arranged in a Y-shape with baselines ranging from 34 to 331 m. We used the CLIMB beam combiner (ten Brummelaar et al. 2013) to combine the K' -band light from three telescopes at a time. Our observations are listed in Tables 3 and 4, with the UT and heliocentric Julian dates, the telescope combination used, and the number of visibilities and closure phases (CP) measured. The CLIMB data were reduced with the pipeline developed by J. D. Monnier, with the general method described in Monnier et al. (2011) and

extended to three beams (e.g., Kluska et al. 2018), resulting in squared visibilities (V^2) for each baseline and CP for each closed triangle. We corrected for any instrumental and atmospheric effects on the observed visibilities using observations of stars with known angular diameters taken before and after the target to complete an observation “bracket.” The calibrator stars for HD 8374 were HD 8774 and HD 9616, which have K -band uniform disk angular diameters of 0.38 ± 0.01 mas and 0.38 ± 0.01 mas from Search-Cal (Chelli et al. 2016). The calibrators for HD 24546 were HD 25642 and HD 27084, which have K -band angular diameters of 0.48 ± 0.03 mas and 0.40 ± 0.04 mas.

3.3. PTI Observations

We also observed HD 8374 using the Palomar Testbed Interferometer (PTI; Colavita et al. 1999) from 1999 to 2005 as listed in Table 3. PTI had three 40 cm telescopes with separations of 87–110 m and combined the near-infrared light from two telescopes at a time. The single baseline measured only squared visibilities, because at least three baselines are needed to measure CP. All of the observations were taken in the K band, except on 1999 September 3 which were taken in the H band. These data were reduced using the standard PTI reduction pipeline (Colavita 1999) and calibrated using the software provided by NExSci.¹⁵ The observed calibrator stars were HD 6920, HD 7034, HD 7964, and HD 11007 with K -band angular diameters of 0.58 ± 0.02 mas (van Belle et al. 2008), 0.51 ± 0.02 mas (Boden et al. 2006), 0.42 ± 0.04 mas (Boden et al. 2006), and 0.45 ± 0.10 mas (Konacki & Lane 2004), respectively.

3.4. Binary Positions

We measured the relative positions from the interferometric visibilities and CP using the method¹⁶ of Schaefer et al. (2016) as described in Lester et al. (2019a). Briefly, we searched across a grid of separations in R.A. and decl. for the best-fit relative position. At each grid point, we compared the observed

¹⁴ <https://www.gemini.edu/sciops/instruments/lopeke-zorro/>

¹⁵ <http://nexsci.caltech.edu/software/>

¹⁶ <http://www.chara.gsu.edu/analysis-software/binary-grid-search>

Table 3
Observing Log for HD 8374

UT Date	HJD-2,400,000	Source	Telescope Configuration	Number of V^2	Number of CP
1999 Aug 11	51401.975	PTI	N-S	7	...
1999 Aug 23	51413.988	PTI	N-S	4	...
1999 Sep 3	51424.932	PTI	N-S	5	...
1999 Oct 13	51464.836	PTI	N-S	4	...
1999 Oct 20	51471.808	PTI	N-S	5	...
1999 Oct 26	51477.806	PTI	N-S	6	...
2001 Aug 27	52148.972	PTI	S-W	6	...
2001 Aug 30	52151.973	PTI	S-W	6	...
2001 Sep 25	52177.884	PTI	S-W	6	...
2005 Aug 12	53594.977	PTI	S-W	6	...
2005 Aug 19	53601.963	PTI	S-W	8	...
2005 Oct 23	53666.784	PTI	S-W	7	...
2005 Nov 14	53688.717	PTI	N-S	12	...
2005 Nov 15	53689.679	PTI	N-W	5	...
2017 Sep 7	58003.862	CHARA	E1-W1-W2	12	4
2017 Nov 30	58087.624	CHARA	S1-W1-E1	9	3
2018 Aug 15	58345.929	CHARA	S1-W1-E1	12	4
2018 Aug 16	58346.811	CHARA	S1-W1-E1	21	7
2018 Aug 17	58347.889	CHARA	S1-W1-E1	18	6
2018 Sep 3	58364.787	CHARA	S1-W1-E1	12	4
2018 Sep 4	58365.783	CHARA	S1-W1-E1	9	3
2019 Sep 16	58742.869	CHARA	S1-W1-E1	12	4
2019 Sep 17	58743.836	CHARA	S1-W1-E1	12	4
2019 Sep 18	58744.818	CHARA	S1-W1-E1	12	4

Table 4
Observing Log for HD 24546

UT Date	HJD-2,400,000	Source	Telescope Configuration	Number of V^2	Number of CP
2017 Sep 7	58003.984	CHARA	E1-W1-W2	12	4
2017 Sep 8	58004.982	CHARA	S1-W1-E1	24	8
2017 Oct 11	58037.975	CHARA	S1-W1-E1	21	7
2017 Nov 30	58087.753	CHARA	S1-W1-E1	15	5
2018 Aug 17	58348.009	CHARA	S1-W1-E1	9	3
2019 Sep 17	58743.993	CHARA	S1-W1-E1	18	6
2019 Sep 18	58744.912	CHARA	S1-W1-E1	12	4
2019 Dec 20	58837.781	CHARA	S1-W1-E1	18	6
2019 Dec 21	58838.653	CHARA	S1-W1-E1	18	6

V^2 and CP to model values to fit for the flux ratio and calculate the χ^2 value. We then searched a small area around the best-fit position to fit an ellipse to the contour marking $\chi^2 \leq \chi_{\min}^2 + 1$, which determines the major axis, minor axis, and position angle of the error ellipse. Because the orbital periods of these systems are quite long, any orbital motion within a single night is typically within the error ellipses. The best-fit relative positions, error ellipse parameters, and flux ratio estimates for each night are listed in Tables 5 and 6. The average K' -band flux ratio from the CHARA observations is 0.79 ± 0.14 for HD 8374 and 0.92 ± 0.17 for HD 24546, where the uncertainty corresponds to the standard deviation from all nights.

The PTI observations of HD 8374 used only one baseline per night, so only one vector component of the separation could be measured. This resulted in multiple solutions within the $1\sigma \chi^2$ limit, especially on nights with fewer than five V^2 points. Without CP to measure the flux asymmetry, each solution is also reflected across the origin. In order to break these ambiguities, one could

either fit the visual orbit directly to the visibilities (e.g., Boden et al. 1999; Helminiak et al. 2012), or use the three-telescope observations as a reference. We opted for the latter method and chose the PTI solutions most consistent with a preliminary visual orbit from the CHARA observations.

3.5. Combined Visual + Spectroscopic Solution

We determined the final orbital solution by simultaneously fitting the interferometric and spectroscopic data using the method of Schaefer et al. (2016). The full set of orbital parameters includes the orbital period (P), epoch of periastron (T), eccentricity (e), longitude of periastron of the primary star (ω_1), the inclination (i), the angular semimajor axis (a), the longitude of the ascending node (Ω), the systemic velocity (γ), and the velocity semi-amplitudes (K_1, K_2). Table 7 lists the best-fit orbital solutions for HD 8374 and HD 24546. The visual orbits are shown in Figure 2, and the spectroscopic orbits

Table 5
Relative Positions for HD 8374

UT Date	HJD-2,400,000	Orbital Phase	ρ (mas)	θ (deg)	σ_{maj} (mas)	σ_{min} (mas)	ϕ (deg)	f_2/f_1
1999 Aug 11	51401.9750	0.25	5.632	31.62	0.258	0.062	75.0	0.59
1999 Aug 23	51413.9880	0.59	7.807	354.79	0.604	0.080	99.1	0.45
1999 Sep 3	51424.9322	0.90	3.784	310.03	0.307	0.043	105.7	0.46
1999 Oct 13	51464.8361	0.03	1.927	140.55	1.258	0.141	110.2	0.43
1999 Oct 20	51471.8083	0.23	5.248	37.21	0.986	0.185	111.0	1.00
1999 Oct 26	51477.8062	0.40	7.160	10.10	0.873	0.200	102.2	1.00
2001 Aug 27	52148.9729	0.37	7.307	15.29	0.754	0.061	154.4	0.88
2001 Aug 30	52151.9740	0.46	7.656	7.86	1.702	0.070	149.3	0.64
2001 Sep 25	52177.8845	0.19	4.608	45.12	0.356	0.109	131.6	0.50
2005 Aug 12	53594.9778	0.26	5.673	32.72	0.738	0.068	163.6	0.44
2005 Aug 19	53601.9639	0.46	7.716	8.00	0.377	0.025	166.2	0.83
2005 Oct 23	53666.7841	0.29	6.488	23.88	0.420	0.021	160.5	0.56
2005 Nov 14	53688.7174	0.91	3.259	308.58	0.203	0.023	119.6	0.97
2005 Nov 15	53689.6795	0.94	2.562	296.05	1.016	0.111	89.9	0.95
2017 Sep 7	58003.8658	0.91	3.218	302.72	0.454	0.028	170.9	0.75
2017 Nov 30	58087.6281	0.28	5.921	28.32	0.087	0.037	53.8	0.68
2018 Aug 15	58345.9310	0.59	7.827	355.95	0.390	0.129	154.5	0.72
2018 Aug 16	58346.8129	0.61	7.531	354.32	0.209	0.148	116.8	0.65
2018 Aug 17	58347.8908	0.64	7.667	351.17	0.133	0.136	180.0	0.87
2018 Sep 3	58364.7905	0.12	3.450	69.81	0.022	0.019	4.0	0.79
2018 Sep 4	58365.7858	0.15	3.943	57.84	0.057	0.025	136.3	0.98
2019 Sep 16	58742.8731	0.81	5.905	332.33	0.201	0.201	131.9	0.65
2019 Sep 17	58743.8404	0.84	5.347	328.28	0.049	0.018	166.5	0.98
2019 Sep 18	58744.8179	0.86	4.566	322.29	0.238	0.110	134.6	1.01

Table 6
Relative Positions for HD 24546

UT Date	HJD-2,400,000	Orbital Phase	ρ (mas)	θ (deg)	σ_{maj} (mas)	σ_{min} (mas)	ϕ (deg)	f_2/f_1
2017 Sep 7	58003.9840	0.80	5.385	200.28	0.323	0.040	169.6	0.87
2017 Sep 8	58004.9818	0.83	4.663	209.18	0.083	0.064	69.7	0.90
2017 Oct 11	58037.9752	0.91	2.983	258.48	0.139	0.078	55.6	0.69
2017 Nov 30	58087.7533	0.55	9.733	168.72	0.328	0.089	3.5	0.79
2018 Aug 17	58348.0094	0.10	4.635	125.20	0.114	0.087	73.9	0.96
2019 Sep 17	58743.9935	0.11	5.082	128.84	0.108	0.073	140.6	0.65
2019 Sep 18	58744.9119	0.14	6.167	135.93	0.088	0.088	15.5	1.00
2019 Dec 20	58837.7811	0.19	7.961	143.18	0.098	0.059	145.65	0.50
2019 Dec 21	58838.6529	0.22	8.549	146.10	0.164	0.073	129.71	0.66

are shown in Figure 3. To determine the uncertainty of each orbital parameter, we performed a Monte Carlo error analysis in which we varied each data point within its Gaussian uncertainty and refit for the orbital solution. We then made a histogram of the best-fit parameters from 10^5 iterations and fit Gaussians to each distribution to determine the 1σ uncertainties in each parameter (listed in Table 7).

4. Stellar Parameters

4.1. Masses and Distance

From the visual and spectroscopic orbital solution, we calculated the masses and distances of HD 8374 and HD 24546 using the nominal solar values from Prša et al. (2016). All of the fundamental stellar parameters for HD 8374 and HD 24546 are listed in Table 8. We found HD 8374 to have masses of $M_1 = 1.636 \pm 0.050 M_\odot$ and $M_2 = 1.587 \pm 0.049 M_\odot$, and a distance of $d = 61.7 \pm 0.7$ pc. The distance from our orbital parallax is consistent with the Gaia DR2 (Gaia Collaboration et al. 2016)

Table 7
Orbital Parameters from VB+SB2 Solution

Parameter	HD 8374	HD 24546
P (days)	35.36836 ± 0.00005	30.43885 ± 0.00002
T (HJD-2400000)	54293.208 ± 0.004	57340.551 ± 0.003
e	0.6476 ± 0.0005	0.6421 ± 0.0006
ω_1 (deg)	325.18 ± 0.10	207.71 ± 0.11
i (deg)	140.64 ± 0.45	56.76 ± 0.45
a (mas)	5.05 ± 0.02	6.99 ± 0.06
Ω (deg)	336.2 ± 0.1	150.2 ± 0.3
γ (km s $^{-1}$)	14.14 ± 0.02	25.43 ± 0.04
K_1 (km s $^{-1}$)	39.27 ± 0.05	52.24 ± 0.06
K_2 (km s $^{-1}$)	40.47 ± 0.05	53.15 ± 0.06

distance of 62.5 ± 0.6 pc (Bailer-Jones et al. 2018) from its trigonometric parallax. For HD 24546, we found masses of $M_1 = 1.434 \pm 0.014 M_\odot$ and $M_2 = 1.409 \pm 0.014 M_\odot$, and a distance of $d = 38.7 \pm 0.2$ pc. This is also consistent with the

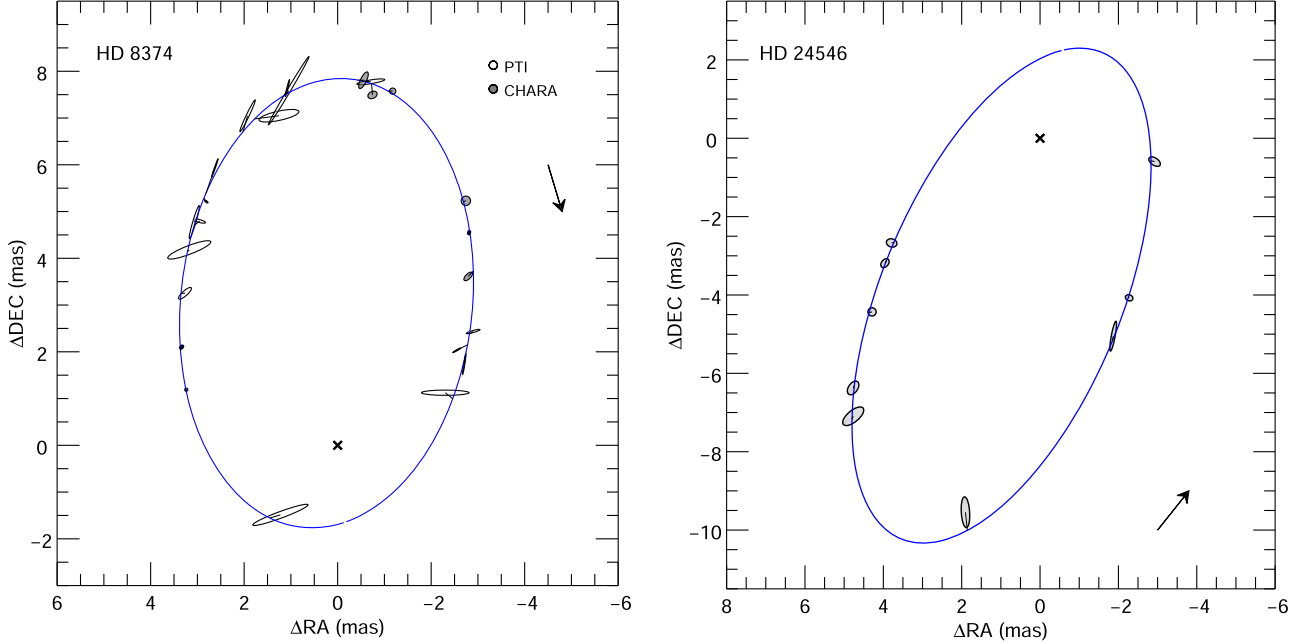


Figure 2. Visual orbit of HD 8374 (left) and HD 24546 (right). The primary star is located at the origin (black cross), and the relative positions of the secondary star are marked by the gray, filled ellipses (CHARA) and the open ellipses (PTI) corresponding to the size of the error ellipses. Several of the PTI data points have a very large axis ratio and appear as line segments. The solid blue curve represents the best-fit model visual orbit, and a thin black line connects each observed and model position. The arrow indicates the direction of orbital motion.

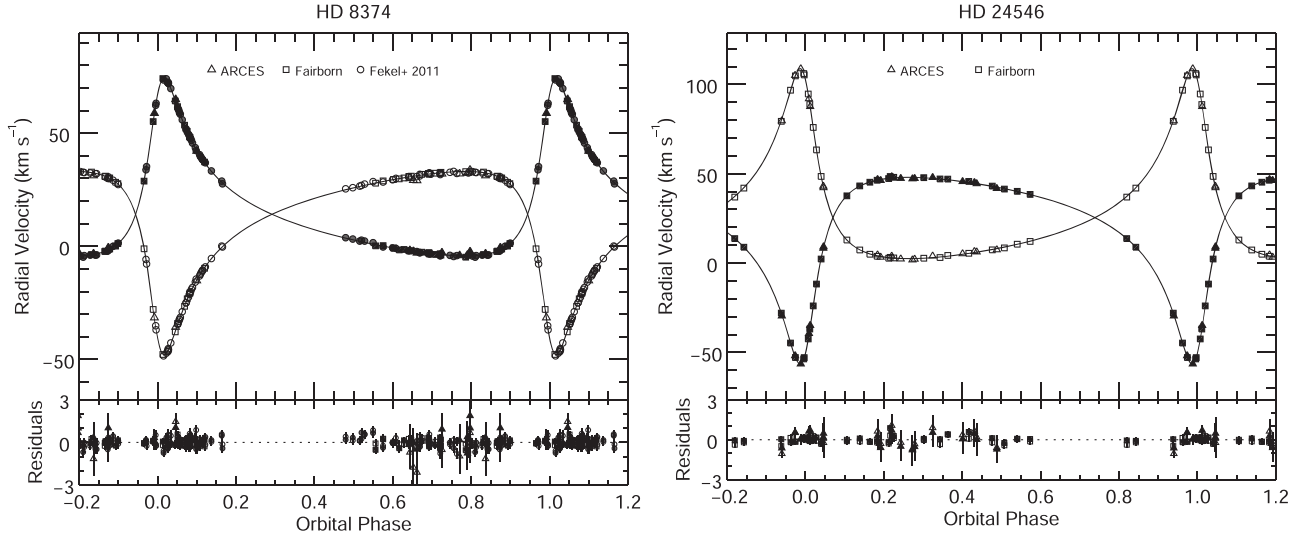


Figure 3. Radial velocity curve of HD 8374 (left) and HD 24546 (right). The observed data for the primary and secondary star are shown with the filled and open points, respectively. The model curves are shown with the solid lines, and the residuals to the fit are shown in the bottom panels.

Gaia DR2 distance of 38.4 ± 0.2 pc for HD 24546 (Bailer-Jones et al. 2018).

4.2. Effective Temperatures and Rotational Velocities

To determine the atmospheric parameters of these stars, we first reconstructed the individual spectrum of each component using a Doppler tomography algorithm (Bagnuolo et al. 1992) with BLUERED template spectra as inputs. We then compared the reconstructed spectra to model spectra of various effective temperatures (T_{eff}) and projected rotational velocities ($V \sin i$). For each combination of T_{eff} and $V \sin i$, we calculated the CCF of the model and reconstructed spectra at several echelle orders featuring strong metal absorption lines. We added the CCFs from all orders together to form a grid of CCFs as a function of T_{eff} and

$V \sin i$, then interpolated within the grid to find the CCF maximum position and the corresponding best-fit T_{eff} and $V \sin i$ for each component. For HD 8374, we found $T_{\text{eff}\,1} = 7280 \pm 110$ K, $T_{\text{eff}\,2} = 7280 \pm 120$ K, $V_1 \sin i = 15.9 \pm 1.3$ km s $^{-1}$, and $V_2 \sin i = 15.2 \pm 1.4$ km s $^{-1}$. Both components are rotating faster than their pseudosynchronous velocities of 9.6 and 8.7 km s $^{-1}$. For HD 24546, we found $T_{\text{eff}\,1} = 6790 \pm 120$ K, $T_{\text{eff}\,2} = 6770 \pm 90$ K, $V_1 \sin i = 14.1 \pm 0.9$ km s $^{-1}$, and $V_2 \sin i = 10.6 \pm 0.7$ km s $^{-1}$. Both components are rotating close to their pseudosynchronous velocities (Hilditch 2001) of 12.9 and 12.4 km s $^{-1}$. Figure 4 shows the reconstructed spectra of each component and the model spectra created using these best-fit atmospheric parameters. Extended figure sets are included in the Appendix.

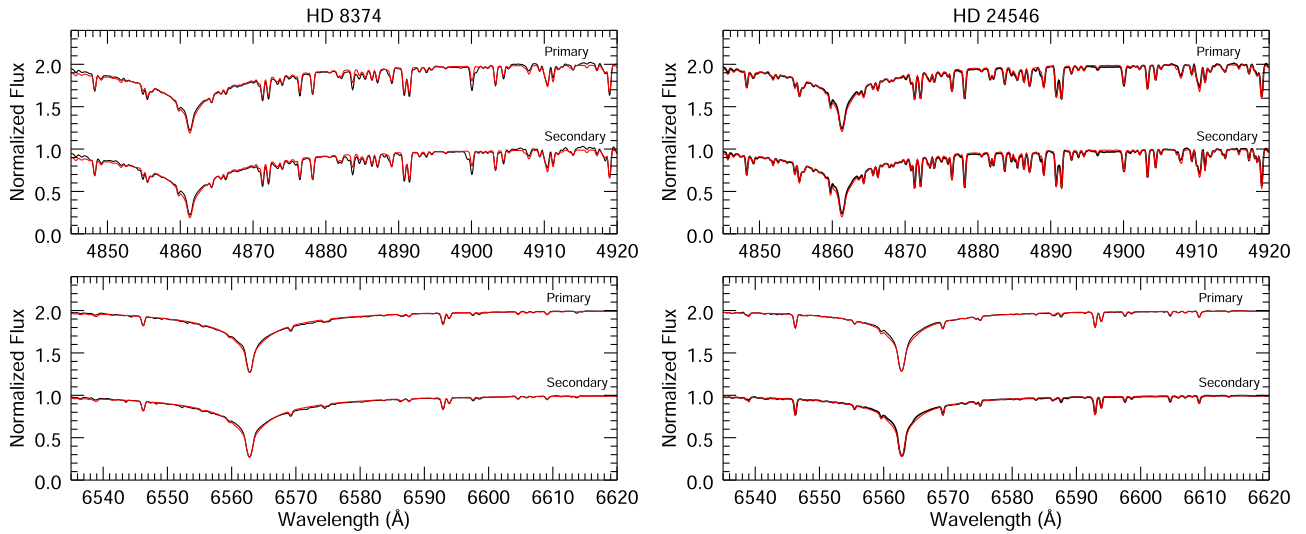


Figure 4. Reconstructed spectra of HD 8374 (left) and HD 24546 (right) around H β and H α . The reconstructed spectra are shown in black, and the best-fit model spectra are overplotted in red.

Table 8
Stellar Parameters

Parameter	HD 8374	HD 24546
$M_1 (M_\odot)$	1.636 ± 0.050	1.434 ± 0.014
$M_2 (M_\odot)$	1.587 ± 0.049	1.409 ± 0.014
$R_1 (R_\odot)$	1.84 ± 0.05	1.67 ± 0.06
$R_2 (R_\odot)$	1.66 ± 0.12	1.60 ± 0.10
$T_{\text{eff} 1}$ (K)	7280 ± 110	6790 ± 120
$T_{\text{eff} 2}$ (K)	7280 ± 120	6770 ± 90
$\log g_1$ (cgs)	4.16 ± 0.02	4.15 ± 0.02
$\log g_2$ (cgs)	4.22 ± 0.03	4.18 ± 0.03
$V_1 \sin i$ (km s $^{-1}$)	15.9 ± 1.3	14.1 ± 0.9
$V_2 \sin i$ (km s $^{-1}$)	15.2 ± 1.4	10.6 ± 0.7
Distance (pc)	61.7 ± 0.7	38.7 ± 0.2
$E(B - V)$ (mag)	0.04 ± 0.01	0.07 ± 0.02

4.3. Radii and Surface Gravities

We gathered photometry from the literature to create spectral energy distributions (SEDs) of HD 8374 and HD 24546, including ultraviolet fluxes from TD-1 (Thompson et al. 1978), optical fluxes from Soubiran et al. (2016), and infrared fluxes from the Two Micron All Sky Survey (2MASS; Skrutskie et al. 2006) and the Wide-field Infrared Survey Explorer (WISE; Wright et al. 2010). We then created a binary SED model using

$$f_\lambda = \frac{1}{d^2} (R_1^2 F_{\lambda 1} + R_2^2 F_{\lambda 2}) \times 10^{-0.4A_\lambda}$$

where $F_{\lambda 1}$ and $F_{\lambda 2}$ are surface flux models of each component (Castelli & Kurucz 2004), R_1 and R_2 are the stellar radii, d is the distance, and A_λ is the extinction in magnitudes. We used the reddening curves (R_λ) of Fitzpatrick (1999) to calculate the extinction at each wavelength for a given color excess, where $A_\lambda = R_\lambda \times E(B - V)$. We also calculated the radius ratio (R_2/R_1) of each system from the model surface flux ratio and the observed flux ratios near H α (from the spectroscopic flux ratio) and in the K' band (from the interferometric flux ratio).

The weighted-average radius ratio is then $R_2/R_1 = 0.91 \pm 0.06$ for HD 8374 and $R_2/R_1 = 0.96 \pm 0.05$ for HD 24546.

We substituted this ratio into the above equation, then fit the binary model SED to the observed fluxes in order to determine R_1 and A_λ (reported in terms of $E(B - V)$ in Table 8). We calculated R_2 from the radius ratios and calculated the surface gravities ($\log g$) from the masses and radii. For HD 8374, we found $R_1 = 1.84 \pm 0.05 R_\odot$, $R_2 = 1.66 \pm 0.12 R_\odot$, $\log g_1 = 4.04 \pm 0.01$, and $\log g_2 = 4.11 \pm 0.03$. For HD 24546, we found $R_1 = 1.67 \pm 0.06 R_\odot$, $R_2 = 1.60 \pm 0.10 R_\odot$, $\log g_1 = 4.15 \pm 0.02$, and $\log g_2 = 4.18 \pm 0.03$. The observed fluxes and the best-fit binary SED model are shown in Figure 5.

4.4. Comparison with Evolutionary Models

To estimate the ages of HD 8374 and HD 24546, we compared the observed stellar parameters to the predictions of the evolutionary models from Yonsei-Yale Y^2 (Demarque et al. 2004) and from Modules for Experiments in Stellar Astrophysics (MESA; Paxton et al. 2011, 2013, 2015, 2018, 2019). The Yonsei-Yale Y^2 models were made for each component with their interpolation program.¹⁷ These models adopt a mixing length parameter of $\alpha_{\text{ML}} = 1.74$, which corresponds to the mixing length divided by the local pressure scale height. The Y^2 models also use a step function prescription for the convective core overshooting, where the overshooting parameter (α_{ov}) increases from 0.0 to 0.2 based on the star's mass. The MESA models¹⁸ were created at the observed masses with MESA release 10108. The default mixing length parameter is $\alpha_{\text{ML}} = 2.0$ for these models. We also chose overshooting parameters of $f_{\text{ov}} = 0.01$ for both components of HD 8374 and $f_{\text{ov}} = 0.005$ for both components of HD 24546 based on the empirical calibration of Claret & Torres (2018). Both sets of models are also non-rotating and use solar metallicity.

Finally, we estimated the age of each binary system by averaging the individual component ages (where the model most closely matches the observed parameters), and determined the uncertainty from the range of ages that match the parameters of both components. For HD 8374, we found the

¹⁷ <http://www.astro.yale.edu/demarque/yystar.html>

¹⁸ <http://www.mesa.sourceforge.net/index.html>

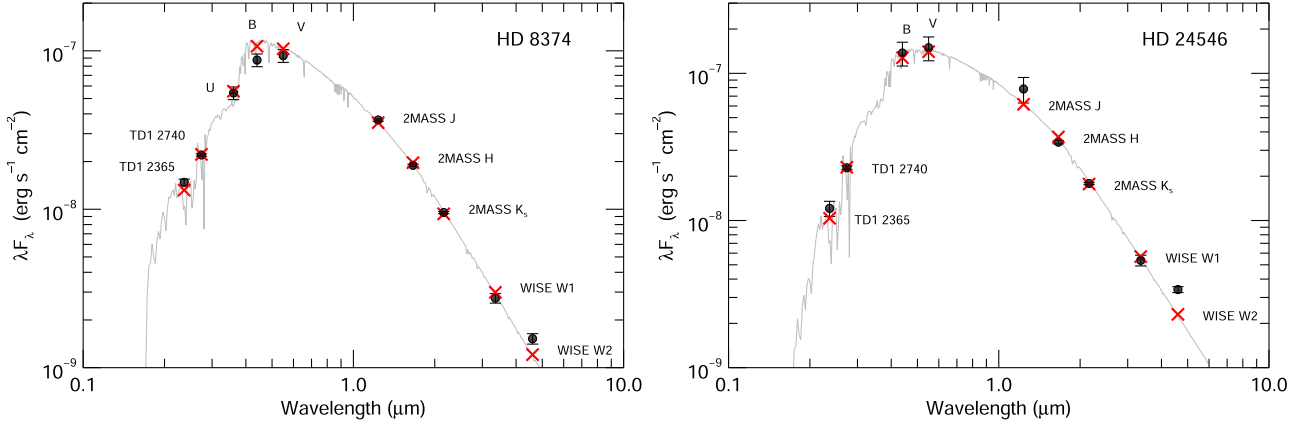


Figure 5. SED of HD 8374 (left) and HD 24546 (right). The observed fluxes are shown in black, and the best-fit binary model fluxes are shown as the red crosses. The full binary model is shown in gray.

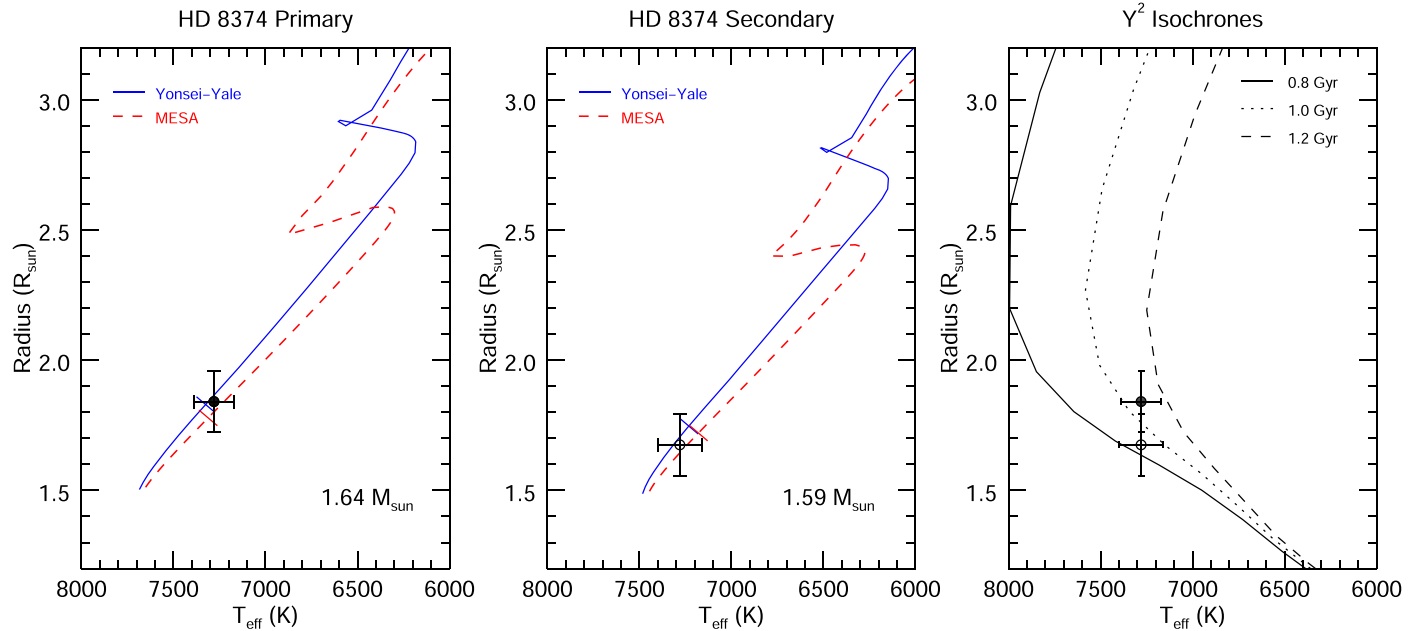


Figure 6. Evolutionary tracks (left, center) and isochrones (right) for HD 8374. The observed stellar parameters are shown as the filled points for the primary star and open points for the secondary star. The Yonsei-Yale models are shown as solid blue lines and the MESA models are shown as dashed red lines. The orthogonal tick marks represent the position of the mean system age on each track. The Yonsei-Yale Y^2 isochrones for 0.8, 1.0, and 1.2 Gyr are shown in the right panel.

system age to be 1.0 ± 0.1 Gyr in the Y^2 models and 0.8 ± 0.2 Gyr in the MESA models. The evolutionary tracks and isochrones for HD 8374 are shown in Figure 6. The models successfully intersect the observed properties of both components at a single age.

For HD 24546, the Y^2 models successfully intersect the observations at an age of 1.5 ± 0.3 Gyr, as shown in Figure 7. However, the MESA models could not reproduce the observed values at the same age. To solve this problem, we first tested different mixing length parameters from $\alpha_{ML} = 1.8\text{--}2.7$, the range tested by Claret & Torres (2018), to find which tracks intersect the observations with the least difference in age between the components. We found the best value to be $\alpha_{ML} = 2.7$ for both components and a corresponding system age of 1.4 ± 0.2 Gyr. MESA evolutionary tracks for the default value of $\alpha_{ML} = 2.0$ and the best-fit value of $\alpha_{ML} = 2.7$ are shown in Figure 7.

Next, we kept α_{ML} fixed to 2.0 and tested different metallicities from $Z = 0.015\text{--}0.020$, where MESA adopts a solar metallicity of

$Z_\odot = 0.020$ from Grevesse & Sauval (1998). For each metallicity, we refit for the component effective temperatures using the method described in Section 4.2 and model spectra interpolated to the given metallicity. Because the BLUERED spectra use $Z_\odot = 0.019$ from Anders & Grevesse (1989), we used the same $\log(Z/Z_\odot)$ for both models and found that decreasing the ratio by 0.02 dex resulted in a decreased effective temperature by about 50 K, which is within the temperature uncertainties. We found that a slightly subsolar metallicity of $Z = 0.017$ could successfully fit the parameters of both components at an age of 1.3 ± 0.2 Gyr as shown in Figure 8.

5. Discussion

By measuring the visual and spectroscopic orbits of HD 8374 and HD 24546, we determined the masses of each component to within 3% and the radii to within 7%. To better test the stellar evolution models, the next step would be to reduce the uncertainties in stellar radius. Typically, this is done

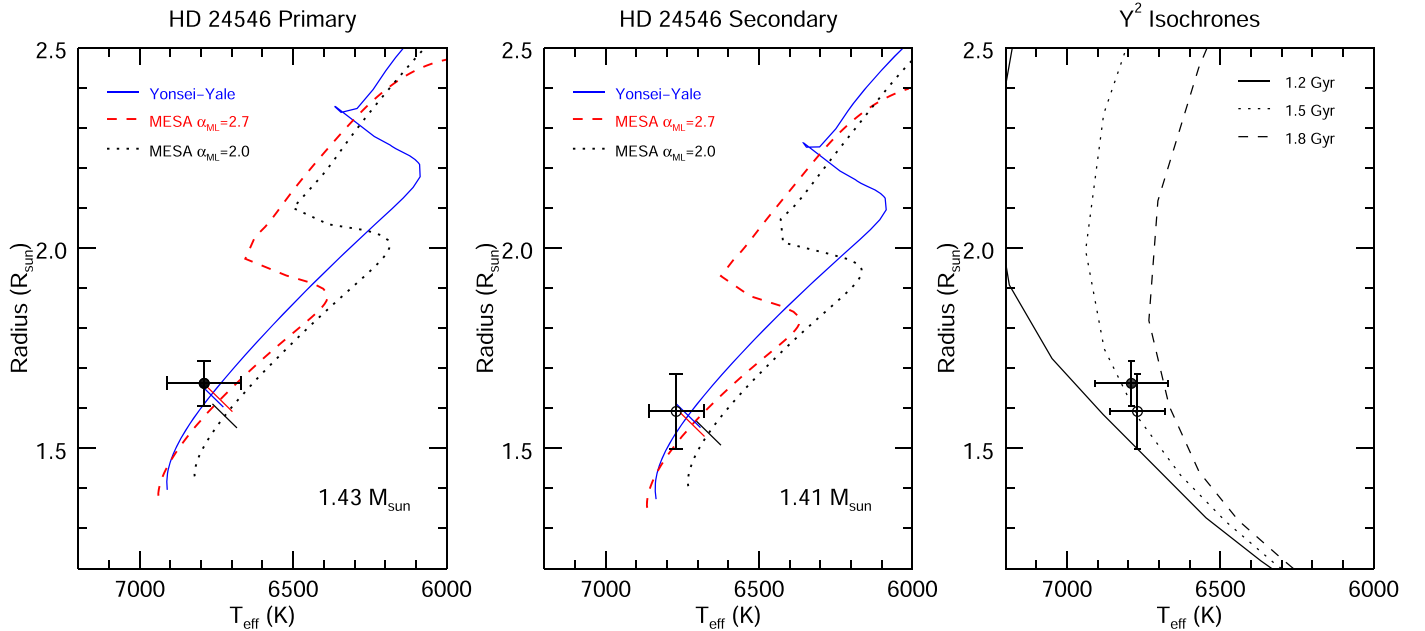


Figure 7. Evolutionary tracks (left, center) and isochrones (right) for HD 24546. The observed stellar parameters are shown as the filled, black points for the primary star and open points for the secondary star. The Yonsei-Yale models are shown as solid blue lines. The MESA models for $\alpha_{ML} = 2.7$ are shown as dashed red lines, while the MESA models for $\alpha_{ML} = 2.0$ are shown as dotted gray lines. The orthogonal tick marks represent the position of the mean system age on each track. The Yonsei-Yale isochrones for 1.2, 1.5, and 1.8 Gyr are shown in the right panel.

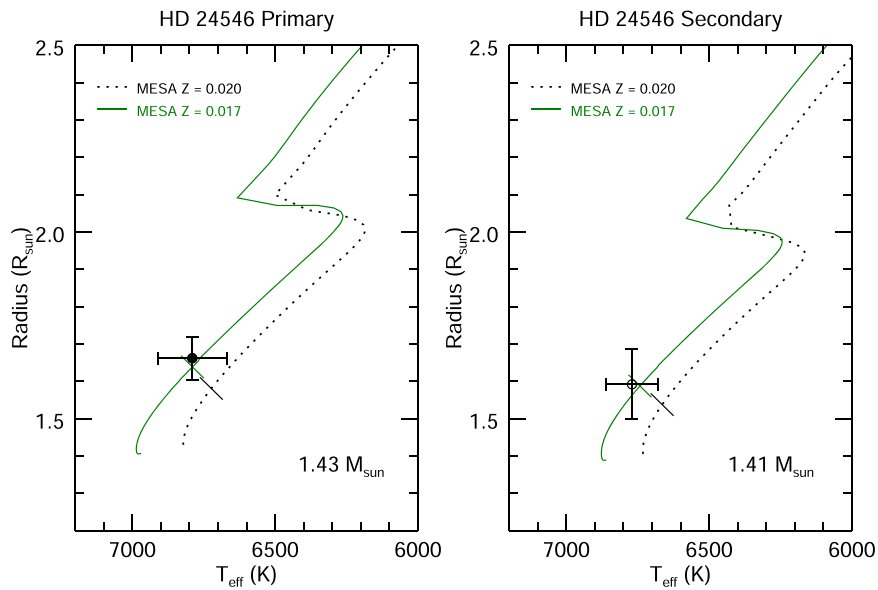


Figure 8. MESA evolutionary tracks for the primary component (left) and the secondary component (right) for two different metallicities. The $Z = 0.017$ models are shown in solid green and the solar $Z = 0.020$ models are shown as black dotted lines. The orthogonal tick marks represent the position of the mean system age on each track.

with light-curve modeling for short-period, eclipsing systems. However, HD 8374 and HD 24546 have periods of 30 or more days, orbital inclinations far from 90 degrees, and radii less than twice that of the Sun, so neither HD 8374 nor HD 24546 is expected to show eclipses.

Therefore, better radius estimates can only be measured by resolving the component stars with long-baseline interferometry at visible wavelengths. The Precision Astronomical Visible Observations (PAVO; Ireland et al. 2008) and Visible spElectroGraph and polArimeter (VEGA; Mourard et al. 2009) beam combiners at CHARA currently have angular resolutions

of 0.25 mas and 0.20 mas, respectively, and the Naval Precision Optical Interferometer (NPOI; Armstrong et al. 1998) is expected to have an angular resolution of 0.15 mas when the 432 m baseline is installed. The components of HD 8374 have estimated angular diameters of 0.29 and 0.26 mas, while the components of HD 24546 have estimated angular diameters of 0.40 and 0.38 mas, so both arrays would be able to resolve the individual stars within these systems.

We also confirm that both components of HD 8374 show much weaker Ca II lines than found in the model spectra of an early F-type star, as seen in Figure A1. This is consistent with

other Am stars, which are defined by an apparent surface under-abundance of calcium (Conti 1970). The metal and hydrogen line depths of HD 8374 appear to match the models, so these abundances are likely close to solar.

Finally, we report on whether or not HD 24546 is a member of the Hyades cluster. The cluster distance is 48.3 ± 2.0 pc at the center with an estimated radius of 10 pc (Perryman et al. 1998). We found the distance of HD 24546 to be 38.6 ± 0.4 pc, consistent with the inner edge of the Hyades cluster. However, our age for HD 24546 from the Y^2 evolutionary tracks is 1.5 ± 0.3 Gyr, compared to ages for the Hyades cluster of 625 ± 50 Myr using non-rotating models (Perryman et al. 1998) or 750 ± 100 Myr using rotating models (Brandt & Huang 2015). The BANYAN code of Gagné et al. (2018) also reports 0% probability of cluster membership using positions, proper motions, radial velocities, and parallaxes. Thus, we conclude that HD 24546 is not a member of the Hyades cluster.

The authors would like to thank the staff at APO and CHARA for their invaluable support during observations, as well as Joel Eaton for collecting some of the TSU 2 m AST spectra. Institutional support has been provided from the GSU College of Arts and Sciences and the GSU Office of the Vice President for Research and Economic Development. Astronomy at Tennessee State University (TSU) is supported by the state of Tennessee through its Centers of Excellence Program. J.D.M. acknowledges funding from NASA NNX09AB87G. This work is based in part upon observations obtained with the Apache Point Observatory 3.5 m telescope, owned and operated by the Astrophysical Research Consortium; the Georgia State University Center for High Angular Resolution

Astronomy Array at Mount Wilson Observatory, supported by the National Science Foundation under grants No. AST-1636624 and AST-1715788; the Palomar Testbed Interferometer, operated by the NASA Exoplanet Science Institute and the PTI collaboration and developed by the Jet Propulsion Laboratory, California Institute of Technology with funding provided from the National Aeronautics and Space Administration; and the High-Resolution Imaging instrument ‘Alopeke at Gemini-North (GN-2018B-FT-102), funded by the NASA Exoplanet Exploration Program and built at the NASA Ames Research Center by Steve B. Howell, Nic Scott, Elliott P. Horch, and Emmett Quigley. This work has also made use of the Jean-Marie Mariotti Center SearchCal service, the CDS Astronomical Databases SIMBAD and VIZIER, the Wide-field Infrared Survey Explorer, and the Two Micron All Sky Survey.

Facilities: APO:3.5 m, CHARA, Gemini:North, PO:PTI, TSU:AST.

Software: Grid Search for Binary Stars (Schaefer et al. 2016), MESA (Paxton et al. 2011), RVFIT (Iglesias-Marzoa et al. 2015), SearchCal (Chelli et al. 2016), TODCOR (Zucker & Mazeh 1994), Y^2 models (Demarque et al. 2004).

Appendix

This appendix includes figure sets showing the reconstructed and model spectra of HD 8374 and HD 24546 (Figures A1 and A2). Each figure contains panels for three different echelle orders featuring strong absorption lines in the range of 3930–6640 Å. The model spectra were created from BLUE-RED models corresponding to the atmospheric parameters listed in Table 8 and solar metallicity.

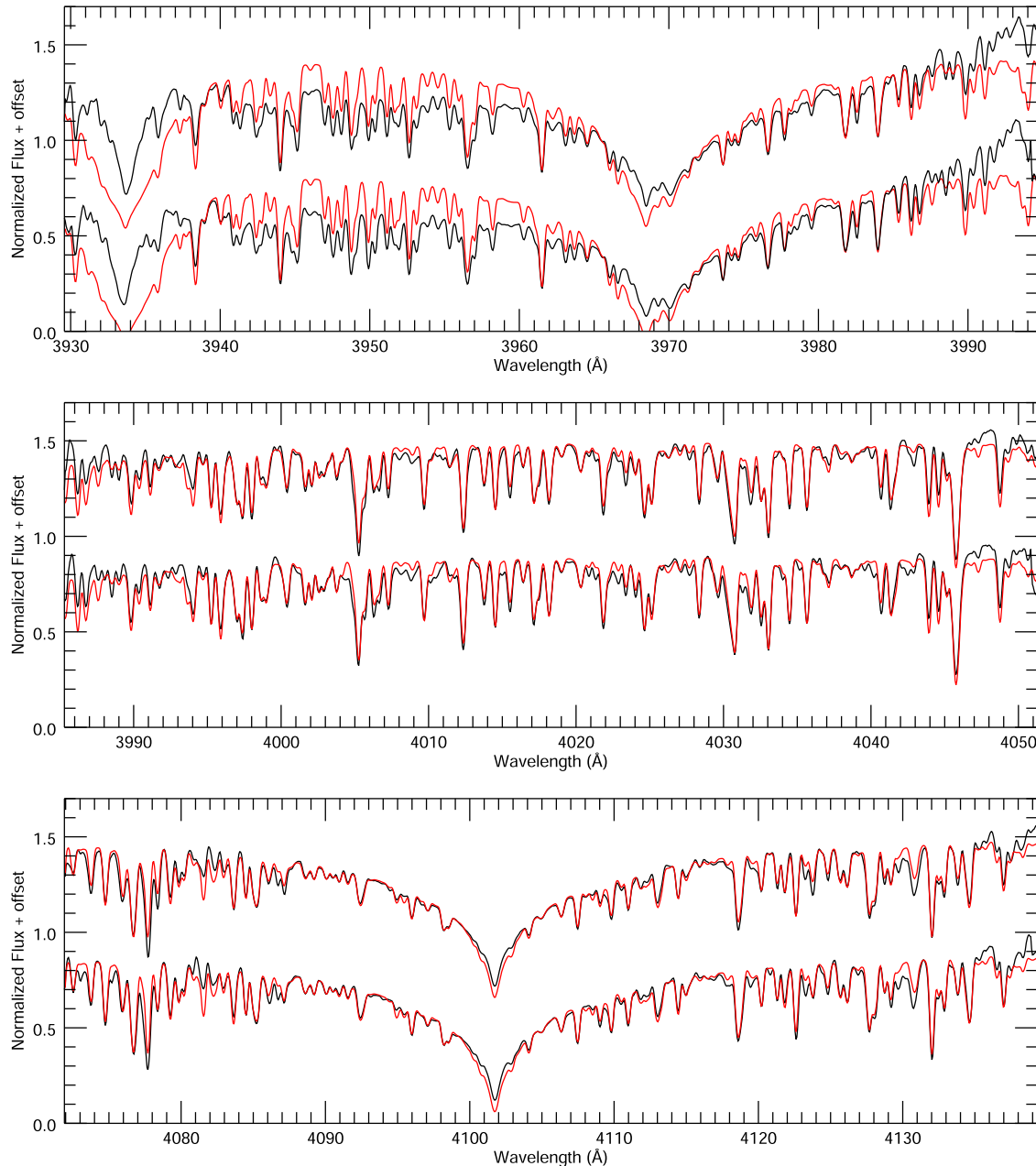


Figure A1. Reconstructed spectra of HD 8374 are shown in black for the primary component (top) and secondary component (bottom). The best-fit model spectra are shown in red.

(The complete figure set (8 images) is available.)

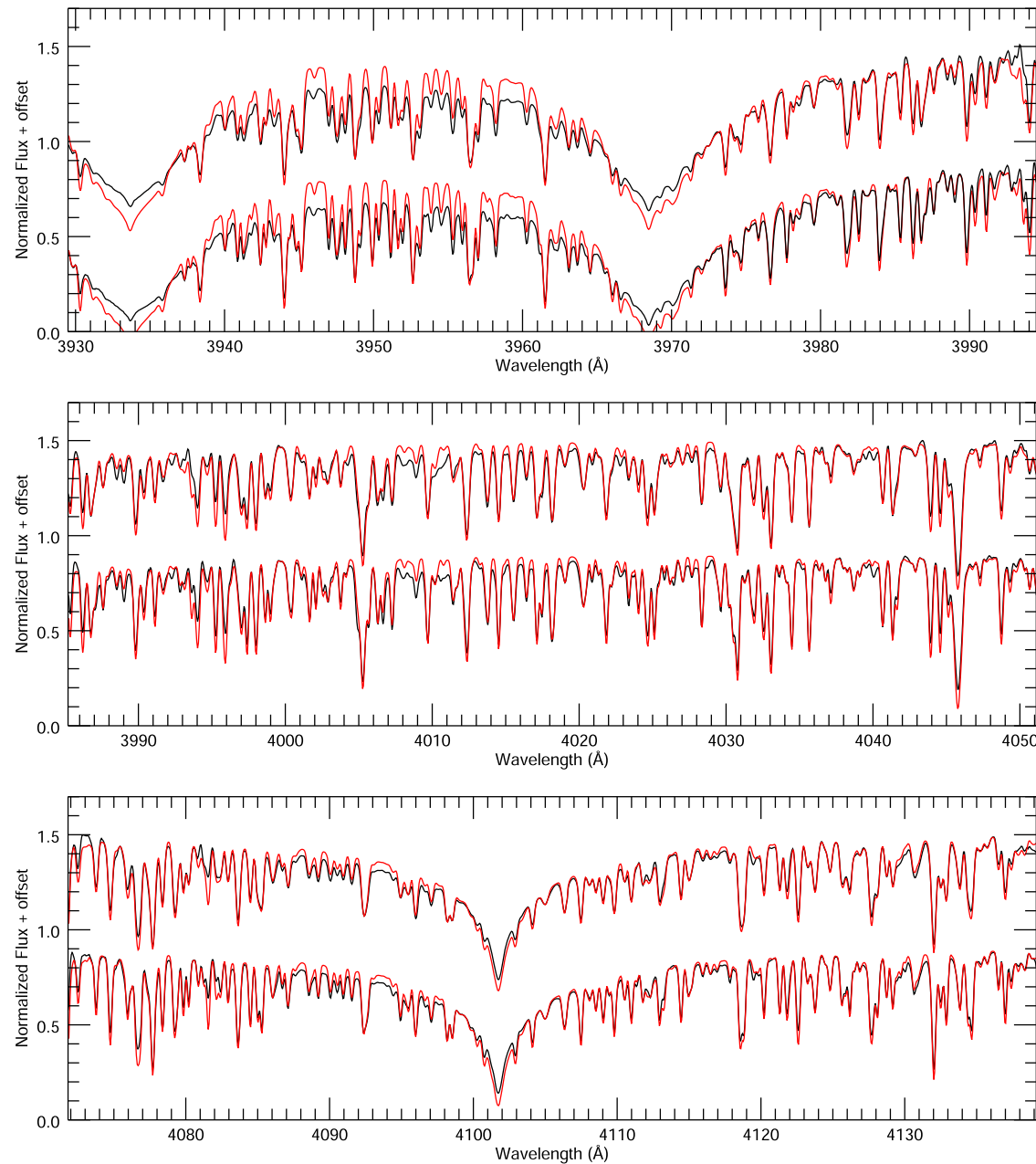


Figure A2. Reconstructed spectra of HD 24546 are shown in black for the primary component (top) and secondary component (bottom). The best-fit model spectra are shown in red.

(The complete figure set (8 images) is available.)

ORCID iDs

- Kathryn V. Lester [ID](https://orcid.org/0000-0002-9903-9911)
 Francis C. Fekel [ID](https://orcid.org/0000-0002-9413-3896)
 Douglas R. Gies [ID](https://orcid.org/0000-0001-8537-3583)
 Gail H. Schaefer [ID](https://orcid.org/0000-0001-5415-9189)
 Christopher D. Farrington [ID](https://orcid.org/0000-0001-9939-2830)
 Zhao Guo [ID](https://orcid.org/0000-0002-0951-2171)
 Rachel A. Matson [ID](https://orcid.org/0000-0001-7233-7508)
 John D. Monnier [ID](https://orcid.org/0000-0002-3380-3307)
 Theo ten Brummelaar [ID](https://orcid.org/0000-0002-0114-7915)

References

- Abt, H. A., & Levy, S. G. 1976, *ApJS*, **30**, 273
 Abt, H. A., & Morrell, N. I. 1995, *ApJS*, **99**, 135
 Anders, E., & Grevesse, N. 1989, *GeCoA*, **53**, 197
 Armstrong, J. T., Mozurowich, D., Rickard, L. J., et al. 1998, *ApJ*, **496**, 550
 Baguado, W. G., Jr., Gies, D. R., & Wiggs, M. S. 1992, *ApJ*, **385**, 708
 Bailer-Jones, C. A. L., Rybizki, J., Fouesneau, M., et al. 2018, *AJ*, **156**, 58
 Bertone, E., Buzzoni, A., Chávez, M., & Rodríguez-Merino, L. H. 2008, *A&A*, **485**, 823
 Boden, A. F., Koresko, C. D., van Belle, G. T., et al. 1999, *ApJ*, **515**, 356
 Boden, A. F., Torres, G., & Latham, D. W. 2006, *ApJ*, **644**, 1193
 Brandt, T. D., & Huang, C. X. 2015, *ApJ*, **807**, 58
 Castelli, F., & Kurucz, R. L. 2004, in Proc. IAU Symp. 210, Modelling of Stellar Atmospheres, ed. N. Piskunov, W. W. Weiss, & D. F. Gray (San Francisco, CA: ASP), **A20**
 Chelli, A., Duvert, G., Bourgès, L., et al. 2016, *A&A*, **589**, A112
 Claret, A., & Torres, G. 2018, *ApJ*, **859**, 100
 Colavita, M. M. 1999, *PASP*, **111**, 111
 Colavita, M. M., Wallace, J. K., Hines, B. E., et al. 1999, *ApJ*, **510**, 505
 Conti, P. S. 1970, *PASP*, **82**, 781
 Demarque, P., Woo, J.-H., Kim, Y.-C., & Yi, S. K. 2004, *ApJS*, **155**, 667
 Eaton, J. A., & Williamson, M. H. 2004, *Proc. SPIE*, **5496**, 710
 Eaton, J. A., & Williamson, M. H. 2007, *PASP*, **119**, 886
 Eggen, O. J. 1971, *PASP*, **83**, 741
 Fekel, F. C., Rajabi, S., Mutterspaugh, M. W., et al. 2013, *AJ*, **145**, 111
 Fekel, F. C., Tomkin, J., & Williamson, M. H. 2009, *AJ*, **137**, 3900
 Fekel, F. C., Tomkin, J., Williamson, M. H., et al. 2011, *AJ*, **142**, 69
 Fitzpatrick, E. L. 1999, *PASP*, **111**, 63
 Fletcher, J. M. 1967, *JRASC*, **61**, 56
 Gagné, J., Mamajek, E. E., Malo, L., et al. 2018, *ApJ*, **856**, 23
 Gaia Collaboration, Prusti, T., de Bruijne, J. H. J., et al. 2016, *A&A*, **595**, A1
 Grevesse, N., & Sauval, A. J. 1998, *SSRv*, **85**, 161
 Helminiak, K. G., Konacki, M., Mutterspaugh, M. W., et al. 2012, *MNRAS*, **419**, 1285
 Hilditch, R. W. 2001, An Introduction to Close Binary Stars (Cambridge: Cambridge Univ. Press)
 Horch, E. P., Casetti-Dinescu, D. I., Camarata, M. A., et al. 2017, *AJ*, **153**, 212
 Howell, S. B., Everett, M. E., Sherry, W., Horch, E., & Ciardi, D. R. 2011, *AJ*, **142**, 19
 Iglesias-Marzoa, R., López-Morales, M., & Jesús Arévalo Morales, M. 2015, *PASP*, **127**, 567
 Ireland, M. J., Mérand, A., ten Brummelaar, T. A., et al. 2008, *Proc. SPIE*, **7013**, 701324
 Kluska, J., Kraus, S., Davies, C. L., et al. 2018, *ApJ*, **855**, 44
 Kolbas, V., Pavlovski, K., Southworth, J., et al. 2015, *MNRAS*, **451**, 4150
 Konacki, M., & Lane, B. F. 2004, *ApJ*, **610**, 443
 Lépine, S., & Bongiorno, B. 2007, *AJ*, **133**, 889
 Lester, K. V., Gies, D. R., Schaefer, G. H., et al. 2019a, *AJ*, **157**, 140
 Lester, K. V., Gies, D. R., Schaefer, G. H., et al. 2019b, *AJ*, **158**, 218
 Monnier, J. D., Zhao, M., Pedretti, E., et al. 2011, *ApJL*, **742**, L1
 Montes, D., González-Peinado, R., Tabernero, H. M., et al. 2018, *MNRAS*, **479**, 1332
 Mourard, D., Clausse, J. M., Marcotto, A., et al. 2009, *A&A*, **508**, 1073
 Paxton, B., Bildsten, L., Dotter, A., et al. 2011, *ApJS*, **192**, 3
 Paxton, B., Cantiello, M., Arras, P., et al. 2013, *ApJS*, **208**, 4
 Paxton, B., Marchant, P., Schwab, J., et al. 2015, *ApJS*, **220**, 15
 Paxton, B., Schwab, J., Bauer, E. B., et al. 2018, *ApJS*, **234**, 34
 Paxton, B., Smolec, R., Schwab, J., et al. 2019, *ApJS*, **243**, 10
 Perryman, M. A. C., Brown, A. G. A., Lebreton, Y., et al. 1998, *A&A*, **331**, 81
 Prša, A., Harmanec, P., Torres, G., et al. 2016, *AJ*, **152**, 41
 Sandberg Lacy, C. H., & Fekel, F. C. 2011, *AJ*, **142**, 185
 Scarfe, C. D. 2010, *Obs*, **130**, 214
 Schaefer, G. H., Hummel, C. A., Gies, D. R., et al. 2016, *AJ*, **152**, 213
 Scott, N. J., Howell, S. B., Horch, E. P., et al. 2018, *PASP*, **130**, 054502
 Skrutskie, M. F., Cutri, R. M., Stiening, R., et al. 2006, *AJ*, **131**, 1163
 Soubiran, C., Le Campion, J.-F., Brouillet, N., et al. 2016, *A&A*, **591**, A118
 ten Brummelaar, T. A., McAlister, H. A., Ridgway, S. T., et al. 2005, *ApJ*, **628**, 453
 ten Brummelaar, T. A., Sturmann, J., Ridgway, S. T., et al. 2013, *JAI*, **2**, 1340004
 Thompson, G. I., Nandy, K., Jamar, C., et al. 1978, Catalogue of Stellar Ultraviolet Fluxes: A Compilation of Absolute Stellar Fluxes Measured by the Sky Survey Telescope (S2/68) aboard the ESRO Satellite TD-1 (1st ed.; London: The Science Research Council)
 Tokovinin, A. A. 1997, *A&AS*, **124**, 75
 van Belle, G. T., van Belle, G., Creech-Eakman, M. J., et al. 2008, *ApJS*, **176**, 276
 Wallerstein, G. 1973, *PASP*, **85**, 115
 Wang, S.-i., Hildebrand, R. H., Hobbs, L. M., et al. 2003, *Proc. SPIE*, **4841**, 1145
 Wright, E. L., Eisenhardt, P. R. M., Mainzer, A. K., et al. 2010, *AJ*, **140**, 1868
 Zucker, S., & Mazeh, T. 1994, *ApJ*, **420**, 806
 Zucker, S., Mazeh, T., Santos, N. C., Udry, S., & Mayor, M. 2003, *A&A*, **404**, 775